

Viologen-Immobilized 2D Polymer Film Enabling Highly Efficient Electrochromic Device for Solar-Powered Smart Window

Zhiyong Wang, Xiangkun Jia, Panpan Zhang, Yannan Liu, Haoyuan Qi, Peng Zhang, Ute Kaiser, Sebastian Reineke,* Renhao Dong,* and Xinliang Feng*

Electrochromic devices (ECDs) have emerged as a unique class of optoelectronic devices for the development of smart windows. However, current ECDs typically suffer from low coloration efficiency (CE) and high energy consumption, which have thus hindered their practical applications, especially as components in solar-powered EC windows. Here, the high-performance ECDs with a fully crystalline viologen-immobilized 2D polymer (V2DP) thin film as the color-switching layer is demonstrated. The high density of vertically oriented pore channels (pore size ≈ 4.5 nm; pore density $\approx 5.8 \times 10^{16} \text{ m}^{-2}$) in the synthetic V2DP film enables high utilization of redox-active viologen moieties and benefits for Li^+ ion diffusion/transport. As a result, the as-fabricated ECDs achieve a rapid switching speed (coloration, 2.8 s; bleaching, 1.2 s), and a high CE ($989 \text{ cm}^2 \text{ C}^{-1}$), and low energy consumption ($21.1 \mu\text{W cm}^{-2}$). Moreover, it is managed to fabricate transmission-tunable, self-sustainable EC window prototypes by vertically integrating the V2DP ECDs with transparent solar cells. This work sheds light on designing electroactive 2D polymers with molecular precision for optoelectronics and paves a practical route toward developing self-powered EC windows to offset the electricity consumption of buildings.

applications in smart windows/mirrors, battery charge sensors, and displays.^[1] In particular, with the increasing demand for efficient energy usage, energy-saving buildings using EC smart windows have garnered the most attention. This is because the EC smart windows are capable of regulating the transmission of visible and near-infrared light under potential bias, allowing building energy use savings up to 40%.^[1a,2] To meet this application need, developing highly efficient ECDs is in great demand. So far, a broad variety of EC materials have been explored in recent years, including metal oxides (WO_3 , V_2O_5 , and NiO),^[3] metal complexes (Prussian blue),^[4] small molecules (viologen and its derivatives),^[5] and conducting polymers (polypyrrole, polythiophene, and polyaniline).^[6] Typically, WO_3 has been widely investigated as a known inorganic EC material due to its excellent stability, fast switching speed,

high coloration contrast, and low energy consumption.^[7] Over the past decades, significant improvements in the performance have been a result of producing amorphous and nanostructured WO_3 to realize high porosity and active surface area, which can

1. Introduction


Electrochromic devices (ECDs) are a unique type of optoelectronic device with customizable optical properties and potential

Z. Wang, P. Zhang, Y. Liu, H. Qi, P. Zhang, R. Dong, X. Feng
Center for Advancing Electronics Dresden (cfaed) and Faculty
of Chemistry and Food Chemistry, Technische Universität Dresden
01062 Dresden, Germany

E-mail: renhao.dong@tu-dresden.de; xinliang.feng@tu-dresden.de

Z. Wang

Institute of Physical Chemistry and Polymer Physics,
Leibniz-Institut für Polymerforschung Dresden e. V.
01069 Dresden, Germany

 The ORCID identification number(s) for the author(s) of this article can be found under <https://doi.org/10.1002/adma.202106073>.

© 2021 The Authors. Advanced Materials published by Wiley-VCH GmbH. This is an open access article under the terms of the Creative Commons Attribution-NonCommercial-NoDerivs License, which permits use and distribution in any medium, provided the original work is properly cited, the use is non-commercial and no modifications or adaptations are made.

DOI: 10.1002/adma.202106073

X. Jia, S. Reineke
Dresden Integrated Center for Applied Physics and Photonic Materials
(IAPP) and Institute for Applied Physics
Technische Universität Dresden
01187 Dresden, Germany
E-mail: sebastian.reineke@tu-dresden.de

H. Qi, U. Kaiser
Central Facility for Electron Microscopy
Electron Microscopy Group of Materials Science
Universität Ulm
89081 Ulm, Germany

R. Dong
Key Laboratory of Colloid and Interface Chemistry of the Ministry of
Education
School of Chemistry and Chemical Engineering
Shandong University
Jinan 250100, China

X. Feng
Department of Synthetic Materials and Functional Devices, Max Planck
Institute for Microstructure Physics
D-06120 Halle (Saale), Germany

provide efficient channels for Li⁺ diffusion and promote effective EC reactions.^[6b,7a] Recently, owing to the chemical diversity, solution processability, and compatibility with flexible substrates, organic EC materials have emerged as promising candidates for high-performance ECDs.^[8] Among these materials, viologen and its derivatives have evolved as one of the most studied ones because of their low driving voltage, a wide variety of color variations, and low manufacturing cost.^[5a] In this regard, much effort has been devoted to exploring the sophisticated viologen-based EC materials through post-modification of viologens, polymeric viologens, and the construction of composites with inorganic materials.^[5a,b,9] However, the practical use of the viologen-based materials for ECDs is still hampered by their long switching time (>3 s), and low CE (<500 cm² C⁻¹) due to the sluggish ionic diffusion and limited charge transport through the random and chaotic pathways during the switching process. A promising scheme to address these challenges relies on developing viologen-based EC films with ordered channels for fast ion diffusion.

Two-dimensional polymers (2DPs)^[10] and their layer-stacked 2D covalent organic frameworks (2D COFs)^[11] are an emerging class of organic layered materials with well-defined permanent porosity. Thanks to their tailor-made structures and properties, these porous crystalline polymers have exhibited the potential for broad functions in optoelectronics, membrane, catalysis, and energy storage and conversion.^[12] Recent advances have demonstrated that 2D COFs integrated with color-switching, redox-active units such as triphenylamine in the backbones could present reversible color switching and are, therefore, excellent candidates for ECDs.^[13] Nevertheless, these 2D COF-based ECDs have not unleashed their full potential to display high CE (while few examples could reach over 800 cm² C⁻¹)^[13d] due to the random stacking of crystallites and the presence of amorphous defects that lead to restricted ion diffusion. In this regard, achieving related materials with highly ordered and oriented columnar-like pores could provide a large interface area with the electrolyte, high utilization of built-in color-switching components, and fast ion diffusion, which are crucial for realizing a quick and efficient EC switching.^[14]

Herein, we demonstrate the highly efficient ECDs employing a novel viologen-immobilized 2DP (**V2DP**) film as the EC layer. The **V2DP** was synthesized from Schiff-base 2D polycondensation between 1,1'-bis(4-aminophenyl)-[4,4'-bipyridine]-1,1'-dium chloride (**1**) and 2,4,6-trihydroxybenzene-1,3,5-tricarbaldehyde (**2**) on the water surface. The resultant **V2DP** presents as a free-standing, fully crystalline film with a large area (over 100 cm²) and tunable thickness (1–65 nm), comprising a high density of positively charged viologen moieties ($\approx 3.5 \times 10^{26}$ m⁻³) and hexagonal pore channels (pore size ≈ 4.5 nm; pore density $\approx 5.8 \times 10^{16}$ m⁻²). By integrating the **V2DP** film into ECDs, we achieve a high switching speed (coloration, 2.8 s; bleaching, 1.2 s), and a high CE (989 cm² C⁻¹ at 90% of the full switch) and low energy consumption (21.1 μ W cm⁻²). Using cyclic voltammogram (CV) and electrochemical impedance spectrum (EIS), we unveil that the **V2DP** allows higher access to viologen moieties and enhanced Li⁺ ions transport than the amorphous counterpart material. Furthermore, we demonstrate a proof-of-concept energy-saving EC system through stacking transparent solar cell (TSC) and ECD, which is capable of independent

and sustainable operations without an external power source, making it an attractive candidate for self-powered, light-controlled smart windows.

2. Results

We synthesized **V2DP** film by (A₂+B₃)-type 2D polycondensation between compounds **1** and **2**, which is illustrated in **Figure 1a,b**, employing a surfactant monolayer-assisted interfacial synthesis (SMAIS). Specifically, a sodium oleyl sulfate (SOS) monolayer was prepared on the water surface in a beaker (diameter, 12 cm). After 10 min, 2 mL trifluoromethanesulfonic acid (TfOH) (74 μ mol) aqueous solution of **1** (4.8 μ mol) was injected into the water subphase (pH reached 1.5 after the injection). Through the electrostatic interaction, the positively charged **1** could be readily adsorbed underneath the SOS monolayer. After 1 h, 2 mL aqueous solution of **2** (3.2 μ mol) was injected into the water subphase to trigger the 2D polymerization. The reaction was kept at room temperature under the ambient condition for 6 days, which afforded the macroscopic yellow film with a lateral size of ≈ 113 cm² and shiny reflection on the water surface (**Figure 1b**, inset). The resultant **V2DP** film on the water surface was robust enough to be fully transferred onto different substrates for characterizations, such as on indium tin oxide (ITO) and SiO₂/Si substrates, as well as transmission electron microscopy (TEM) grid. The morphological features of **V2DP** film were inspected by scanning electron microscopy (SEM), optical microscopy (OM), and atomic force microscopy (AFM). The **V2DP** film exhibited excellent mechanical stability and could suspend over large holes with a side length of ≈ 25 μ m on a TEM grid (**Figure 1c**). The OM and AFM images revealed a homogeneous film with a thickness of 20 nm (**Figure 1d**; **Figure S1**, Supporting Information). In particular, the film presented an ultra-smooth surface with a root mean square (RMS) roughness of 0.62 nm in an area of 20 \times 20 μ m². Note that the thickness of **V2DP** film could be finely tuned from 1 to 65 nm by controlling the reaction time from 1 day to 40 days (**Figure S2**, Supporting Information).

We further confirmed the bonding information and chemical composition of **V2DP** film by multiple spectroscopy techniques. ATR-FTIR spectra show the vanishing of the characteristic of N–H stretch (≈ 3184 cm⁻¹) from compound **1** and carbonyl stretching band (≈ 1639 cm⁻¹) from compound **2**, respectively (**Figure S3**, Supporting Information), suggesting the efficient conversion of amine and aldehyde groups into imine linkages in **V2DP** film. Besides, a new band at 1655 cm⁻¹ characteristics for –C=N stretching was observed for **V2DP** in the surface-enhanced Raman spectra, supporting the formation of an imine bond (**Figure S4**, Supporting Information). The energy-dispersive X-ray spectroscopy (EDX) mapping (**Figure S5**, Supporting Information) and X-ray photoelectron spectroscopy (XPS) (**Figure S6a–d**, Supporting Information) analysis reveal a homogenous distribution of C, N, O, S, and F in **V2DP**. The observed F1s and S2p signals, combined with the disappearance of Cl2p manifest that the counter ion Cl⁻ in monomer **1** was substituted by CF₃SO₃⁻ after the on-water surface polymerization (**Figure S6e**, Supporting Information).

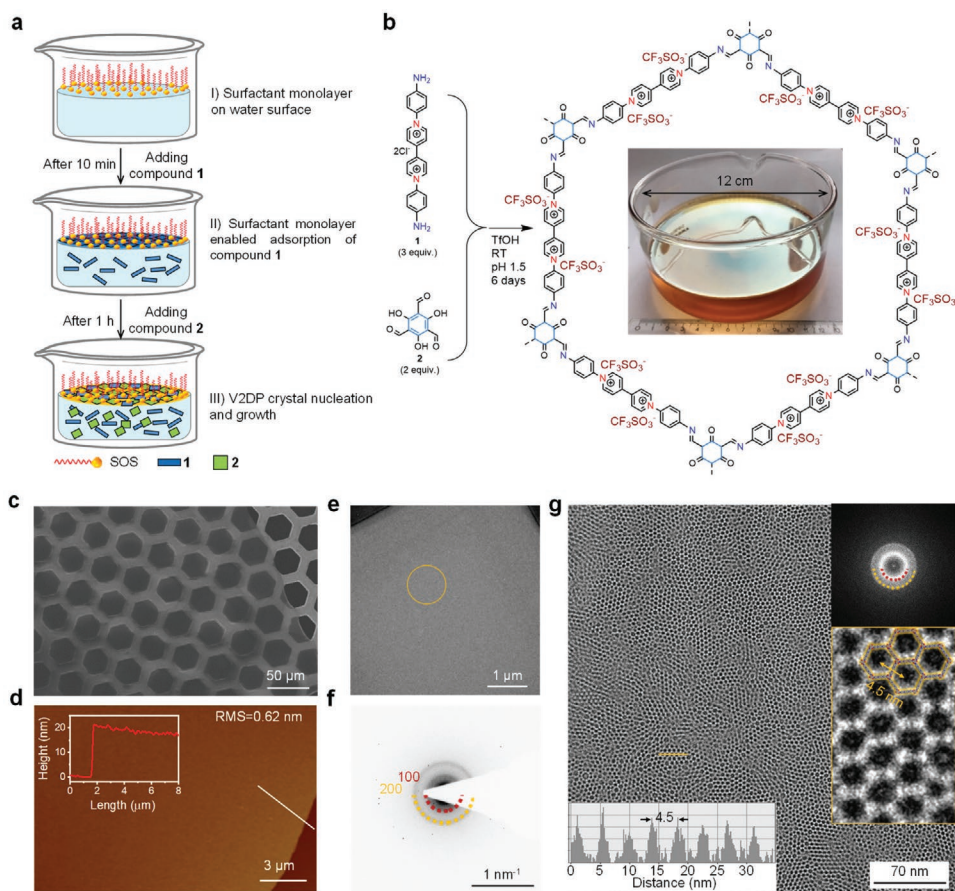


Figure 1. Synthesis protocol and structural characterizations of **V2DP**. a) A schematic of the synthetic procedure through the SMAIS method. b) A reaction scheme illustrating the synthesis of **V2DP** via Schiff-base polycondensation. Inset, OM image of **V2DP** film on the water surface. c) SEM image of **V2DP** film transferred onto a hexagonal copper mesh. d) AFM image and height profile along the white line across **V2DP** film deposited on SiO_2/Si substrate. e) An overview of **V2DP** film by bright-field TEM. f) SAED pattern from the marked position in (e). g) HRTEM image of **V2DP**. Inset, Intensity profiles along the yellow line, FFT, and magnified HRTEM image of **V2DP** with structure overlaid.

To gain insight into the crystallinity and lattice structure of **V2DP**, we performed selected-area electron diffraction (SAED) and high-resolution transmission electron microscopy (HRTEM) imaging. As shown in the SAED pattern, the observed diffraction ring suggests the polycrystalline nature of the synthetic **V2DP** film (Figure 1e,f). The nearest reflection at 0.22 nm^{-1} corresponds to 4.5 nm in real space, agreeing with the lattice parameters of **V2DP**. HRTEM images (Figure 1g; Figure S7, Supporting Information) reveal that the **V2DP** film is fully crystalline with domain sizes of $50\text{--}100 \text{ nm}$ and periodic hexagonal pores with a pore size of 4.5 nm (Figure 1g, inset). To elucidate the layer orientation and stacking in the **V2DP** film on a macroscopic scale, we further performed a synchrotron grazing incidence wide-angle X-ray scattering (GIWAXS) analysis. As shown in Figure S8, Supporting Information, a diffuse arc at $Q_z = 1.68 \text{ \AA}^{-1}$ was observed in the out-of-plane direction, suggesting a preference of **V2DP** for the face-on orientation with a $\pi\text{-}\pi$ stacking distance of 0.37 nm . The in-plane peak at $Q_{xy} = 0.29 \text{ \AA}^{-1}$ corresponds to the 200 Bragg reflections of a hexagonal lattice. The resultant unit cell was assigned with $a = b = 4.5 \text{ nm}$, which is consistent with the lattice structure provided by SAED and HRTEM investigations. These results

unambiguously suggest that the **V2DP** film is face-on oriented with hexagonal channels perpendicular to the substrate, which would provide favorable pathways for ion transport.^[15] For comparison, we also synthesized the contrast sample under the same reaction condition without using surfactant monolayer, which only provided amorphous polyimine (**aPI**) films (Figure S9, Supporting Information).

The electrochemical behavior of the ITO-supported **V2DP** electrode (film thickness, 20 nm) was first evaluated in a 0.1 M LiCl aqueous electrolyte with the CV measurement. As shown in Figure 2a and Figure S10, Supporting Information, the CV curves show two distinct redox peaks at -0.75 V and -0.22 V (vs Ag/AgCl) in a potential window of 0.2 to -1.0 V , corresponding to the reversible two-electron redox reaction of viologen moieties assisted by the insertion/extraction of Li^+ . In Figure 2b, the yellow color of **V2DP** electrode changed to violet at -0.42 V , which was ascribed to the generation of the radical-cation form ($\text{V}^{\bullet+}$) during the first one-electron reduction of the viologen unit (V^{2+}). Then it turned to dark at -0.87 V due to the rapid comproportionation mechanism of the di-reduced form with quinoid structure (**V**).^[5b,c] When the potential increased from -1.0 to 0.2 V , the oxidation of viologen moieties restored

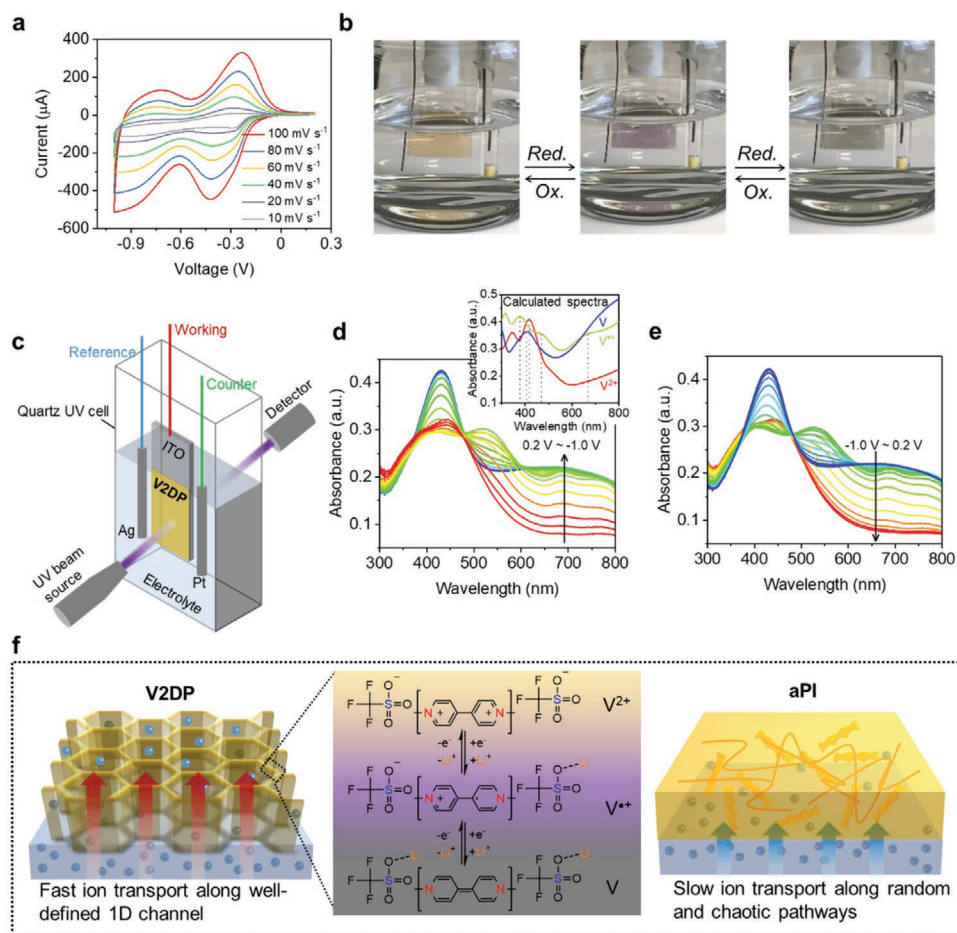


Figure 2. Electrochemical behavior and spectroelectrochemical characterizations. a) CV curves of the **V2DP** electrode at different scan rates from 10 to 100 mV s^{-1} . b) Images of reversible color switching of **V2DP** film. c) Schematic illustration of the in situ spectroelectrochemical measurement. UV-vis spectra changes of **V2DP** electrode recorded during d) reductive and e) oxidative processes. Inset, calculated UV-vis absorption spectra of **V2DP**. f) Schematic of the ion diffusion pathways within the **V2DP** and **aPI** films, as well as the redox mechanism of viologen moiety. For **V2DP**, the high density of vertically oriented pore channels provides high viologen moieties and fast diffusion pathways for Li^+ ions. In contrast, the **aPI** suffers from low ion transport efficiency caused by random diffusion pathways.

the color from dark to violet and ultimately yellow. To further reveal the relationship between the EC performance and corresponding redox reactions in the **V2DP** electrode, UV-vis spectra were real-time recorded during the charge/discharge process (Figure S11, Supporting Information). The in situ UV-vis spectroelectrochemical equipment (Figure 2c) was assembled with an electrochemical workstation and a UV-vis spectroscopy based on a three-electrode system (Pt wire as the counter electrode, Ag wire as the reference electrode, ITO-supported **V2DP** film as the working electrode, and 0.1 M LiCl aqueous electrolyte). During the reduction reaction from 0.2 to -1.0 V, the absorption band at 443 nm proportionally decreased upon one-electron reduction, combined with the increase of the visible absorption region (Figure 2d; Figure S12a, Supporting Information). Meanwhile, new absorption bands emerged at 526 and 688 nm (green spectrum), indicating the formation of a radical-cation form ($\text{V}^{2+} \rightarrow \text{V}^{\bullet+}$). The second reduction commenced at -0.6 V, which generated a dark viologen species that absorbed at 430 nm (blue spectrum), suggesting that the radical-cation form evolved further into the neutral form at the higher bias

voltage ($\text{V}^{\bullet+} \rightarrow \text{V}$). To support the experimental results of the absorption behavior, we further carried out density functional theory (DFT) calculations along with the random phase approximation (RPA) (Figure 2d, inset). Upon one-electron reduction, the calculated UV-vis absorption spectrum of **V2DP** presents new bands at 477 and 670 nm, while the second reduction gives rise to the appearance of the band at 407 nm and the disappearance of bands at 477 and 670 nm. These results support the experimental spectra well, revealing that the observed band shifts are unambiguously associated with the reversible redox reaction of viologen moieties. As shown in Figure 2e and Figure S12b, Supporting Information, the absorption reverted to its original state during the oxidation from -1.0 to 0.2 V. Thus, we can conclude that the different characteristic ionic states of viologen moieties in **V2DP** contribute to the reversible absorbance changes over reduction-oxidation cycles.

To further gain insight into the insertion/extraction of Li^+ during the redox reaction, we conducted the surface-enhanced Raman (SE Raman) and ATR-FTIR measurements on the **V2DP** film at different redox states including its initial state (yellow),

one-electron reduced state (violet), and oxidized state (yellow). As shown in Figure S13a, Supporting Information, compared with the initial state, the Raman bands of SO_3^- in CF_3SO_3^- become broader with lower intensity in the one-electron reduced **V2DP**, indicating that the Li^+ can insert into **V2DP**, and thus be uptook by CF_3SO_3^- to form $\text{CF}_3\text{SO}_3^- \cdots \text{Li}^+$ pairs. As such, ATR-FTIR spectra show relatively broad and weak absorptions at 1255 cm^{-1} (CF_3), and 1172 and 1030 cm^{-1} (SO_3^-) in the one-electron reduced **V2DP** (Figure S13b, Supporting Information). In contrast, these peaks recover to their original states in the oxidized **V2DP**, supporting that the concentration of free CF_3SO_3^- is increased due to the dissociation ionic pairs during the oxidation of viologen moieties. These results reveal that the redox reaction of viologen moieties is associated with the reversible Li^+ uptaking/releasing steps on the CF_3SO_3^- sites.

Due to the fully crystalline nature, **V2DP** film bears the advantage of the high density of built-in viologen moieties in the polymer skeleton ($\approx 3.5 \times 10^{26} \text{ m}^{-3}$) combined with highly ordered and vertically oriented pore channels (pore size $\approx 4.5 \text{ nm}$; pore density $\approx 5.8 \times 10^{16} \text{ m}^{-2}$). In this regard, Li^+ ions from an aqueous electrolyte could efficiently pass through the uninterrupted pores to access the viologen moieties for the redox reactions (Figure 2f). Thus, the ion diffusion and the redox reactions occur throughout the entire **V2DP** structures simultaneously, leading to efficient and fast EC switching. For comparison, we investigated the electrochemical behavior of **aPI** film (thickness $\approx 20 \text{ nm}$) under the same condition. **aPI** film presented a much smaller CV area than its crystalline counterpart, indicating slow ion diffusion and low utilization of accessible viologen moieties (Figure 2f; Figure S14, Supporting Information). Besides, the EIS of **V2DP** and **aPI** films were recorded in the frequency range of 100 kHz to 0.1 Hz (Figure S15, Supporting Information). Notably, unlike the semicircle behavior for **aPI**, the spectrum for **V2DP** displays a straight line with a high slope in the low-frequency range, indicating a more prominent capacitive behavior and lower diffusion resistance of Li^+ ions. **V2DP** has a smaller radius at a high frequency than that of **aPI**, suggesting that the enhanced ion transport originates from the periodic porous structure. These results highlight the substantial contribution of the high porosity and well-defined channels in improved ion transport and highly accessible color-switching units, which play a crucial role in EC performance.

We then constructed a quasi-solid-state **V2DP**-based ECD (**V2DP** ECD), which comprises an ITO-supported **V2DP** working electrode (thickness of **V2DP**, 20 nm), interfaced with a blank ITO glass as the counter electrode via the electrolyte of 0.1 M LiCl-based polyvinyl alcohol (PVA) gel (Figure 3a). Upon applying a negative potential (from -1.4 to -2.1 V) to the working electrode, electron flow from the external circuit into the **V2DP** film, resulting in the reduction of the viologen moieties. This caused a stepwise change of the ECD color from yellow to violet (Figure 3b; Video S1, Supporting Information), accompanied by a gradually reduced average visible-light transmission (AVT) from 70.9% to 50.2% and color rendering index (CRI) from 98 to 89 (Table S1, Supporting Information). Further increasing the potential to -2.3 V led to a dark state, indicating the formation of radical-cations and further evolving into neutral form at higher bias voltages. The CIE 1931 (x, y)

coordinates at bleaching and colored states are shown in Figure S16, Supporting Information. The coloration reaction was reversed upon applying positive potentials from 0.1 to 0.5 V , enabling oxidation of neutral viologen moieties by Li^+ transport from **V2DP** film to the electrolyte, which is consistent with the observation in the electrochemical measurement. Figure 3c,d presents the corresponding transmission spectra at each state. The contrast ratio between yellow and violet states was determined to be $\approx 25\%$ at either 557 or 686 nm , which is well comparable with the reported 2D COF-based EC materials with the thickness of hundreds of nanometers.^[13a,b] It should be noted that this transmission difference value can be increased to 40% when the thickness of **V2DP** film is increased to 40 nm (Figures S17 and S18, Supporting Information). Therefore, we believe that by adjusting the thickness of **V2DP** film, our ECDs can have varied optical contrast values and be used in different environments. As shown in Figure 3e, the transmission of the ECD at 550 nm was recorded when the device was applied with the bias of -2.0 and $+1.0 \text{ V}$. The coloration (t_c) and bleaching (t_b) time for 90% of the transmission change between yellow and violet states were 2.8 and 1.2 s , respectively (Figure 3f). The stability of **V2DP** ECDs was also evaluated, revealing the contrast ratio dropped only $\approx 0.5\%$ for 550 nm after 15 cycles ($\approx 4.4\%$ after 200 cycles) of potential switching (Figure S19, Supporting Information).

Next, we calculated the charge density consumed for optical contrast, that is, CE ,^[16] for both coloration and bleaching processes at 90% , 95% , and 98% of the full switch (Table S2, Supporting Information). Notably, the CE and energy consumption were calculated to be $989 \text{ cm}^2 \text{ C}^{-1}$ and $21.1 \mu\text{W cm}^{-2}$ at 90% of optical contrast, respectively. These values are superior to those of the reported 2D COFs (Figure 3f; Figure S20 and Table S3, Supporting Information), **aPI** (Figure S21, Supporting Information), and well comparable with the state-of-the-art highly efficient EC materials such as WO_3 , viologen, and conducting polymers.^[5a,16b,17] Although the CE diminished with the time approaching the full switch, we still achieved the CE of $811 \text{ cm}^2 \text{ C}^{-1}$ at 95% and $711 \text{ cm}^2 \text{ C}^{-1}$ at 98% of optical change. Besides, when the **V2DP** ECD was bleached from violet to yellow at 1.0 V , the CE is around $500 \text{ cm}^2 \text{ C}^{-1}$ and would keep consistent at 90% , 95% , and 98% of the full switch.

In pursuit of portable and wearable optoelectronic devices,^[2a,18] we also fabricated flexible ECDs. As shown in Figure 3g, we transferred the **V2DP** film onto the ITO-coated polyethylene terephthalate (PET) substrate and utilized another blank ITO/PET, and polymer gel as the counter electrode and electrolyte, respectively.^[2e,19] Benefiting from the intrinsic excellent mechanical stability of **V2DP**, the reversible EC switching under bending was achieved with operating voltages ranging from 2.0 to -3.5 V (Figure 3h; Video S2, Supporting Information). We then investigated the mechanical bending stability of the flexible **V2DP** ECD while the coloration/bleaching transmission spectrum at 550 nm was monitored as a function of the bending cycles (Figure S22, Supporting Information). As shown in Figure 3i, the switching times and CE of the device were determined at various bending cycles, indicating stable switching characteristics after 2000 bending cycles; no significant variation in switching time and CE was observed.

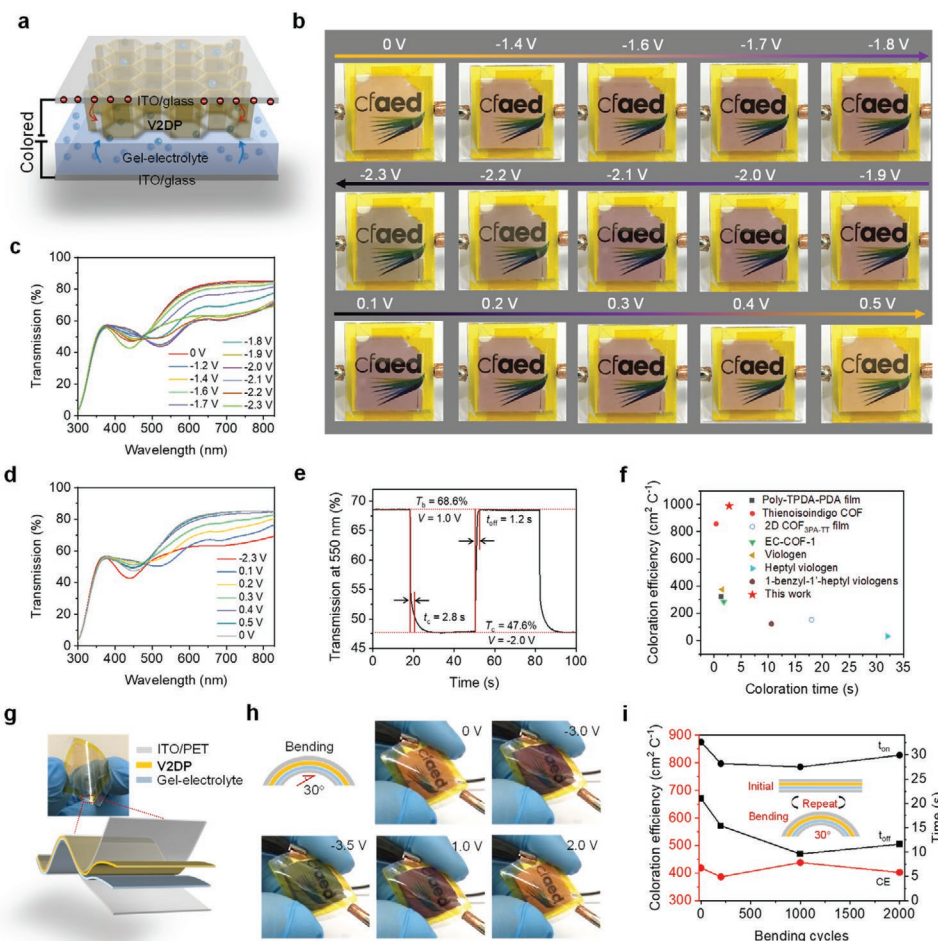


Figure 3. Electrochromic characteristics of the **V2DP** ECDs. a) Schematic illustration of **V2DP** ECD. 0.1 M LiCl-based PVA gel was used as the electrolyte. b) Photographs of reversible color switching of a **V2DP** ECD (device size, 2.88 cm²). The device exhibits color switching from yellow to violet and further to dark at the reductive potentials from 0 to −2.3 V. By applying reverse potentials from 0.1 to 0.5 V, the device was modulated reversely to the initial state. A Keithley 2602 SMU was used to apply voltages to the **V2DP** ECD and to manipulate its transmission properties. Corresponding transmission spectra of a **V2DP** ECD recorded during c) coloration and d) bleaching measurement. e) Coloration/bleaching transmission spectrum at 550 nm for an applied voltage of −2.0/1.0 V, from which switching time and CE were calculated. f) CE as a function of coloration time for ECDs assembled by **V2DP**, and previously reported viologen-based materials, and 2D COFs. g) Schematic illustration of a flexible **V2DP** ECD. h) Images of reversible color switching of the bent flexible **V2DP** ECD at the reductive potentials of −3.0 and −3.5 V, and the oxidative potential of 1.0 and 2.0 V, respectively. i) Switching time and CE of a flexible **V2DP** ECD versus number of applied bending cycles (bending angle, 30°).

The highly efficient **V2DP** ECDs offer the opportunity to fabricate solar-powered EC systems capable of independent and sustainable operations without an external power source, thereby minimizing energy consumption in smart green buildings. As a proof-of-concept demonstration, we further built a solar-powered smart window prototype by vertically integrating the **V2DP** ECD with transparent photovoltaic devices.^[1a,2a,20] As shown in **Figure 4a**, UV-selective absorbing TSCs (active area, 2.52 cm²) with high photovoltages (TSC1, $V_{OC} = 2.0$ V; TSC2, $V_{OC} = 1.6$ V) were used to drive the **V2DP** ECD.^[21] The photovoltaic performance of BF-DPB:B4PYMPM (TSC1) and α -6T/B4PYMPM (TSC2) systems are shown in **Figure 4b,c**, and **Table S5**, Supporting Information. **Figure 4d** details the working principles of the combined devices, in which the outside TSC converts high-energy photons into electric power to regulate the transmission of the **V2DP** ECD in the visible and

NIR region. Characterization of the operation of TSC/ECD stacks is illustrated in **Figure 4e,f**. In TSC1/ECD stack, the ECD was powered by an operating voltage of 2.0 V under around 1 sun intensity. When the applied bias between electrodes was pulsed at negative 2.0 V, the color of the **V2DP** ECD automatically switched from yellow to violet. Concurrently, the AVT of the stack decreased from 29% to 24%, due to the diminished transmission in the range of 480–830 nm (**Figure 4g**). Applying a positive bias drove the **V2DP** ECD toward its bleached transmittance state, and the corresponding AVT quickly resumed to its initial state. Similarly, having TSC2 with a lower V_{OC} of 1.6 V instead of TSC1 was less effective at powering ECD switching (**Figure 4f**), thus leading to a decrease in the transmittance contrast at 550 nm (from 7% to 5%) (**Figure 4h**). Connecting TSC2 and a NIR TSC (TSC3) (**Figure S23**, Supporting Information) with a V_{OC} of 0.7 V in series allows accessing

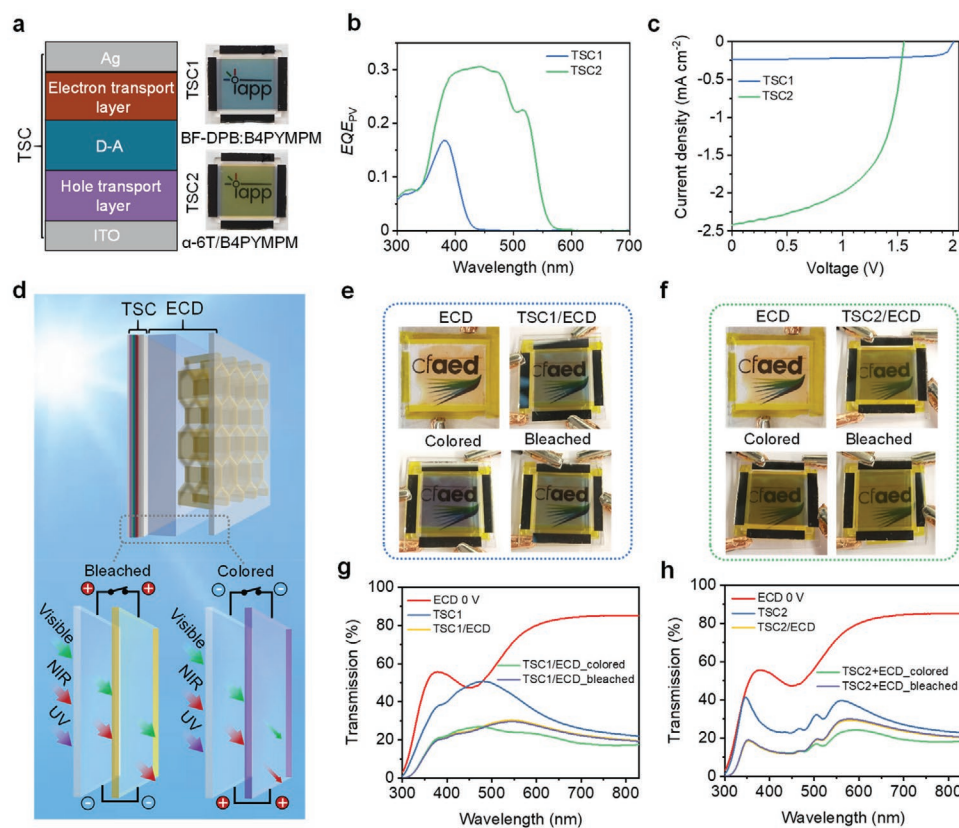


Figure 4. Performance of self-powered TSC/ECD stacks. a) Device configurations and photographs of TSCs based on BF-DPB:B4PYMPM (TSC1) and α -6T/B4PYMPM (TSC2). b) Corresponding external photovoltaic quantum efficiency curves and c) current density–voltage (J – V) characteristics with a top Ag electrode of 15 nm. d) Schematic illustration of TSC/ECD stack in a side-by-side geometry, and working principles of light transmission modulation without competition for the same spectral range. Integration of the TSC with **V2DP** ECD enables to not only automatically switch the device between bleached and colored state when the V_{OC} between electrodes was pulsed at either positive or negative, but also intelligently managed the solar spectrum, with UV light powering the regulation of visible and NIR light. e, f) Photographs of ECD and wire-connected vertical TSC/ECD stacks whose transmission states were manipulated by TSCs under ≈ 1 sun intensity illumination, and g, h) corresponding transmission spectra. It was observed that after combining the **V2DP** ECD with the TSCs, the total transmission was reduced, but the CIE (x , y) coordinates of the stack shifted closer to the reference daylight coordinates (Figure S24, Supporting Information).

a higher V_{OC} of 2.3 V, which is needed for powering a dark state. As shown in Figure S25, Supporting Information, series-connected TSCs under 1 sun intensity enable to switch the **V2DP** ECD reversibly between yellow and dark states. These results demonstrate that the **V2DP** is a promising material for high-performance ECDs that can be vertically integrated with TSC to regulate light absorption under sunlight in real-time, and thus establishing significant potentials for energy-efficient buildings.

3. Conclusion

In conclusion, we demonstrate the highly crystalline viologen-immobilized 2D polymer film (**V2DP**) with a high density of inherent pores and well-defined channels that enable high utilization of viologen moieties and efficient ion transport. On this basis, we fabricated **V2DP**-based ECDs that exhibit a rapid switching speed (coloration, 2.8 s; bleaching, 1.2 s), and a high CE ($989 \text{ cm}^2 \text{ C}^{-1}$ at 90% of the full switch) and low energy consumption ($21.1 \mu\text{W cm}^{-2}$). We further demonstrate that their

pairing with TSCs provides energy-saving EC window systems, which enable the realization of the automatically dynamic light-adjusting, making them compatible with intelligent management of the solar spectrum. Our studies pave the way for the design and synthesis of electroactive 2DP films for superior smart windows, and hence expanding the scope for future energy-efficient buildings.

4. Experimental Section

Synthesis of V2DP through the Surfactant Monolayer Assisted Interfacial Synthesis (SMAIS) Method: 50 mL Milli-Q water was injected into a beaker (160 mL, diameter = 12 cm) to form a static air/water interface. Then, 20 μL SOS (1 mg mL^{-1} in chloroform) was spread onto the surface. The solvent was allowed to evaporate for 10 min, and then 2 mL trifluoromethanesulfonic acid (TfOH) (7.4 μmol) aqueous solution of **1** (4.8 μmol) was gently added to the subphase using the syringe. After 30 min, 2 mL aqueous solution of **2** (3.2 μmol) was added successively. The reaction mixture was then kept undisturbed at room temperature for 6 days. After the polymerization, the synthetic yellow **V2DP** film was deposited onto the substrate by the horizontal dipping method. The

substrate with the V2DP film was dried at 80 °C for 30 min and rinsed with flowing ethanol, Milli-Q water, and then dried in N₂ flow.

Calculation of the Densities of Built-In Viologen Moieties and Pore Channels: The density of built-in viologen moieties can be derived based on the following equation:

$$D_v = \frac{N_{\text{layer}} M_l \frac{A_f}{A_l}}{A_f T} \quad (1)$$

where D_v is the density of viologen moieties, N_{layer} is the number of layers, M_l is the number of viologen in each lattice, A_f is the area of the film, A_l is the area of every lattice and T is the thickness of the film. $N_{\text{layer}} = 40$, $M_l = 3$, $A_f = 113 \text{ cm}^2$, $A_l = 1.73 \times 10^{-17} \text{ m}^2$ and $T = 20 \text{ nm}$, giving rise to $D_v \approx 3.5 \times 10^{26} \text{ m}^{-3}$. In addition, the density of pore channels (D_p) can be calculated to be $\approx 5.8 \times 10^{16} \text{ m}^{-2}$ from the equation of $D_p = \frac{1}{A_l}$.

General Characterization: Optical microscopy (Zeiss), Atomic force microscopy (AFM, NT-MDT), transmission electron microscopy (TEM, Zeiss, Libra 200 KV), and scanning electron microscopy (SEM, Zeiss Gemini 500) equipped with EDX was used to investigate the morphology and structure of the samples. V2DP films were deposited on Si substrate for SEM, and on copper grids for TEM characterizations. All optical microscopy and AFM images were recorded on a 300-nm SiO₂/Si substrate.

UV–vis absorption spectra of the polymers were obtained on a UV–vis–NIR Spectrophotometer Cary 5000 at room temperature. FTIR spectra were collected using Tensor II (Bruker) with an attenuated total reflection (ATR) unit. The samples were prepared by depositing the 2DP films onto a copper foil. X-ray photoelectron spectroscopy (XPS) measurements were carried out using an AXIS Ultra DLD system. Both surveys and high-resolution spectra were collected using a beam diameter of 100 μm. All displayed binding energy values are calibrated to the graphitic C1s peak with a value of 284.6 eV. Thin-film Grazing-incidence wide-angle X-Ray scattering (GIWAXS) data were acquired at European Synchrotron Radiation Facility (ESRF). The photon energy was 10 keV. The focused beam of $\approx 0.3 \times 0.3 \text{ mm}^2$ was directed on the sample at an incident angle α of 0.15° and 0.30°. 2D diffraction patterns were acquired by an X-ray area detector (MarCCD).

Transmission and reflection spectra for ECDs and TSCs were measured by Shimadzu solid-spec 3700 spectrometers. To measure the transmission spectra of EC devices at different applied voltages in Figure 3, the devices were mounted inside the UV–vis spectrometer while being wire-connected to an external power source, a Keithley 2600 SMU. In Figure 4, upon illumination of ≈ 1 sun intensity, self-powered TSC/ECD stacks were tuned to colored states. Since ECDs could stay at color states without power supply, during this period the transmission spectra of self-powered stacks at colored states were measured. With these spectra, optical parameters were calculated.

Electrochemical and In Situ UV Measurement: V2DP film with a thickness of approximately 20 nm was transferred onto an ITO/glass substrate. A standard three-electrode system was assembled by using the prepared V2DP coated ITO/glass as the working electrode, Pt wire as the counter electrode, Ag/AgCl (saturated KCl) as the reference electrode, LiCl aqueous solution (0.1 M) as the electrolyte. Cyclic voltammogram (CV) examined at scan rates of 10–100 mV s⁻¹ was carried out based on a CHI 660E electrochemical workstation.

Computer Calculation: V2DP crystal structure was built using Material Studio 8.0. To optimize the crystal structure and carry out ground-state calculations of V2DP, the density functional theory (DFT) calculation was performed, as implemented in Vienna Ab initio Simulation Package (VASP).^[22] The projector-augmented wave (PAW) method was used to model the interactions between ionic cores and valence electrons. The Perdew–Burke–Ernzhof (PBE) exchange–correlation potentials were employed with an energy cutoff of 520 eV. And Grimme's dispersion (D3) was used for vdW interaction correction.^[23] The ionic and electronic convergence criteria were set as 10⁻⁶ eV and 0.01 eV Å⁻¹, respectively.

The optical absorption of V2DP was calculated using DFT along with the random phase approximation (RPA) as following equations:^[24]

$$\varepsilon(\omega) = \varepsilon^1(\omega) + i\varepsilon^2(\omega) \quad (2)$$

$$I(\omega) = \sqrt{2\omega} \sqrt{|\varepsilon(\omega)| - \varepsilon^1(\omega)} \quad (3)$$

$$|\varepsilon(\omega)| = \sqrt{\varepsilon^1(\omega)^2 + \varepsilon^2(\omega)^2} \quad (4)$$

where $\varepsilon^1(\omega)$ is the real part and $\varepsilon^2(\omega)$ is the imaginary part of the complex dielectric function. $\varepsilon^2(\omega)$ is obtained from summation over electronic states and $\varepsilon^1(\omega)$ is determined using the Kramers–Kronig relationship. $I(\omega)$ is the absorption coefficient and $|\varepsilon(\omega)|$ is the relative dielectric constant.

Assembly of Electrochromic Devices (ECDs): ITO glass (thickness of ITO $\approx 100 \text{ nm}$; resistance, $20 \Omega \square^{-1}$) was cleaned by sequentially washing with Milli-Q water, acetone, and isopropanol. Then, the synthesized V2DP film with a thickness of 20 nm was transferred from the water surface onto the ITO substrate followed by thermal annealing at 80 °C for 30 min, and rinsed with flowing ethanol, Milli-Q water, and then dried in N₂ flow. The polyvinyl alcohol (PVA)/LiCl gel electrolyte was prepared by mixing PVA powder (2.0 g) and LiCl (84.8 mg) in 20 mL deionized water, and heated at 85 °C until the solution became clear. The prepared gel electrolyte was coated on the V2DP film. After that, the V2DP and gel-coated ITO was sealed with another ITO substrate with a double-sided tape spacer. The effective area of ECDs was about 2.88 cm².

Assembly of the Transparent Solar Cell (TSC)/ECD Stacks: The self-powered integrated unit was simply designed by fixing TSC on top of the ECD with tape and these two devices were connected by wires. The fabrication of TSC was as follows. The layers of the small-molecule solar cells were thermally evaporated at ultra-high vacuum (base pressure $< 10^{-7}$ mbar) on a glass substrate with a pre-structured ITO contact. Glass substrates were cleaned in a multi-step wet process including rinsing with *N*-methyl-2-pyrrolidone, ethanol, and deionized water as well as treatment with ultraviolet ozone. All organic materials were purified 2–3 times by sublimation. The device area was defined by the geometrical overlap of the bottom and the top contact, the active area was 2.52 cm². The device structure of TSC1 was: Glass/ITO (90 nm)/NDP9 (1 nm)/BPAPF:NDP9 (10 wt% doping, 25 nm)/BPAPF (5 nm)/BF-DPB:B4PYMPM (1:1 mixing ratio, 30 nm)/BPhen (5 nm)/BPhen:Cs (1:1 wt% doping, 25 nm)/Ca (1 nm)/Ag (15 nm), and that of TSC2 is: Glass/ITO (90 nm)/ α -6T (60 nm)/B4PYMPM (10 nm)/BPhen (5 nm)/BPhen:Cs (1:1 wt% doping, 25 nm)/Ca (1 nm)/Ag (15 nm).

Supporting Information

Supporting Information is available from the Wiley Online Library or from the author.

Acknowledgements

Z.W., X.J., and P.Z. contributed equally to this work. This work was financially supported by EU Graphene Flagship (GrapheneCore3, No. 881603), ERC starting grant (FC2DMOF, No. 852909), ERC Consolidator Grant (T2DCP), Coordination Networks: Building Blocks for Functional Systems (SPP 1928, COORNET), H2020-MSCA-ITN (ULTIMATE, No. 813036), H2020-FETOPEN (PROGENY, 899205), CRC 1415 (Chemistry of Synthetic Two-Dimensional Materials, No. 417590517), as well as the German Science Council and Center of Advancing Electronics Dresden (cfaed). R.D. thanks Taishan Scholars Program of Shandong Province (tsqn201909047). Z.W. and X.J. gratefully acknowledge funding from China Scholarship Council. The authors acknowledge cfaed and Dresden Center for Nanoanalysis (DCN) at TUD and Dr. Petr Formanek, Prof. Andreas Fery for the use of TEM facility at IPF. The authors thank Dr. Zhen Zhang for the XPS measurement, as well as Mr. Dominic Anna Maria for the surface-enhanced Raman testing. The authors also acknowledge the Centre for High Performance Computing (ZIH) in

Dresden, Germany, and the support of computational calculation from Chenghao Liu in McGill University, Canada.

Open access funding enabled and organized by Projekt DEAL.

Conflict of Interest

The authors declare no conflict of interest.

Data Availability Statement

The data that support the findings of this study are available from the corresponding author upon reasonable request.

Keywords

2D polymers, coloration efficiency, electrochromic devices, smart windows

Received: August 4, 2021
Revised: September 26, 2021
Published online:

- [1] a) N. C. Davy, M. Sezen-Edmonds, J. Gao, X. Lin, A. Liu, N. Yao, A. Kahn, Y.-L. Loo, *Nat. Energy* **2017**, *2*, 17104; b) L. Shao, X. Zhuo, J. Wang, *Adv. Mater.* **2018**, *30*, 1704338; c) P. Zhang, F. Zhu, F. Wang, J. Wang, R. Dong, X. Zhuang, O. G. Schmidt, X. Feng, *Adv. Mater.* **2017**, *29*, 1604491.
- [2] a) A. L. Dyer, R. H. Bulloch, Y. Zhou, B. Kippelen, J. R. Reynolds, F. Zhang, *Adv. Mater.* **2014**, *26*, 4895; b) Y. Kim, M. Han, J. Kim, E. Kim, *Energy Environ. Sci.* **2018**, *11*, 2124; c) R. Li, X. Ma, J. Li, J. Cao, H. Gao, T. Li, X. Zhang, L. Wang, Q. Zhang, G. Wang, C. Hou, Y. Li, T. Palacios, Y. Lin, H. Wang, X. Ling, *Nat. Commun.* **2021**, *12*, 1587; d) S. Huang, Y. Liu, M. Jafari, M. Siaj, H. Wang, S. Xiao, D. Ma, *Adv. Funct. Mater.* **2021**, *31*, 2010022; e) K. Wang, H. Wu, Y. Meng, Y. Zhang, Z. Wei, *Energy Environ. Sci.* **2012**, *5*, 8384.
- [3] a) R.-T. Wen, C. G. Granqvist, G. A. Niklasson, *Nat. Mater.* **2015**, *14*, 996; b) S. Cong, F. Geng, Z. Zhao, *Adv. Mater.* **2016**, *28*, 10518; c) H. Gu, C. Guo, S. Zhang, L. Bi, T. Li, T. Sun, S. Liu, *ACS Nano* **2018**, *12*, 559.
- [4] J. Wang, L. Zhang, L. Yu, Z. Jiao, H. Xie, X. W. Lou, X. W. Sun, *Nat. Commun.* **2014**, *5*, 4921.
- [5] a) K. W. Shah, S.-X. Wang, D. X. Y. Soo, J. Xu, *Polymers* **2019**, *11*, 1839; b) C. Kortz, A. Hein, M. Ciobanu, L. Walder, E. Oesterschulze, *Nat. Commun.* **2019**, *10*, 4874; c) G. Li, L. Xu, W. Zhang, K. Zhou, Y. Ding, F. Liu, X. He, G. He, *Angew. Chem., Int. Ed.* **2018**, *57*, 4897.
- [6] a) P. M. Beaujuge, S. Ellinger, J. R. Reynolds, *Nat. Mater.* **2008**, *7*, 795; b) G. Yang, Y.-M. Zhang, Y. Cai, B. Yang, C. Gu, S. X.-A. Zhang, *Chem. Soc. Rev.* **2020**, *49*, 8687; c) P. M. Beaujuge, J. R. Reynolds, *Chem. Rev.* **2010**, *110*, 268.
- [7] a) W. Cheng, J. He, K. E. Dettelbach, N. J. J. Johnson, R. S. Sherbo, C. P. Berlinguette, *Chem* **2018**, *4*, 821; b) W. Wu, M. Wang, J. Ma, Y. Cao, Y. Deng, *Adv. Electron. Mater.* **2018**, *4*, 1800185.
- [8] Q. Zhang, C.-Y. Tsai, L.-J. Li, D.-J. Liaw, *Nat. Commun.* **2019**, *10*, 1239.
- [9] M. R. Geraskina, A. S. Dutton, M. J. Juetten, S. A. Wood, A. H. Winter, *Angew. Chem., Int. Ed.* **2017**, *129*, 9563.
- [10] a) K. Liu, H. Qi, R. Dong, R. Shivhare, M. Addicoat, T. Zhang, H. Sahabudeen, T. Heine, S. Mannsfeld, U. Kaiser, Z. Zheng, X. Feng, *Nat. Chem.* **2019**, *11*, 994; b) W. Liu, X. Luo, Y. Bao, Y. P. Liu, G.-H. Ning, I. Abdelwahab, L. Li, C. T. Nai, Z. G. Hu, D. Zhao, B. Liu, S. Y. Quek, K. P. Loh, *Nat. Chem.* **2017**, *9*, 563; c) G. Galeotti, F. De Marchi, E. Hamzehpoor, O. MacLean, M. Rajeswara Rao, Y. Chen, L. V. Besteiro, D. Dettmann, L. Ferrari, F. Frezza, P. M. Sheverdyayeva, R. Liu, A. K. Kundu, P. Moras, M. Ebrahimi, M. C. Gallagher, F. Rosei, D. F. Perepichka, G. Contini, *Nat. Mater.* **2020**, *19*, 874; d) L. Grill, M. Dyer, L. Laffrentz, M. Persson, M. V. Peters, S. Hecht, *Nat. Nanotechnol.* **2007**, *2*, 687.
- [11] a) C. Gropp, T. Ma, N. Hanikel, O. M. Yaghi, *Science* **2020**, *370*, eabd6406; b) T. Ma, E. A. Kapustin, S. X. Yin, L. Liang, Z. Zhou, J. Niu, L.-H. Li, Y. Wang, J. Su, J. Li, *Science* **2018**, *361*, 48; c) S. Lin, C. S. Diercks, Y.-B. Zhang, N. Kornienko, E. M. Nichols, Y. Zhao, A. R. Paris, D. Kim, P. Yang, O. M. Yaghi, C. J. Chang, *Science* **2015**, *349*, 1208.
- [12] H. Wang, Z. Zeng, P. Xu, L. Li, G. Zeng, R. Xiao, Z. Tang, D. Huang, L. Tang, C. Lai, D. Jiang, Y. Liu, H. Yi, L. Qin, S. Ye, X. Ren, W. Tang, *Chem. Soc. Rev.* **2019**, *48*, 488.
- [13] a) Q. Hao, Z.-J. Li, C. Lu, B. Sun, Y.-W. Zhong, L.-J. Wan, D. Wang, *J. Am. Chem. Soc.* **2019**, *141*, 19831; b) F. Yu, W. Liu, S.-W. Ke, M. Kurmoo, J.-L. Zuo, Q. Zhang, *Nat. Commun.* **2020**, *11*, 5534; c) C.-W. Kung, T. C. Wang, J. E. Mondloch, D. Fairen-Jimenez, D. M. Gardner, W. Bury, J. M. Klingsporn, J. C. Barnes, R. Van Duyn, J. F. Stoddart, M. R. Wasielewski, O. K. Farha, J. T. Hupp, *Chem. Mater.* **2013**, *25*, 5012; d) D. Bessinger, K. Muggli, M. Beetz, F. Auras, T. Bein, *J. Am. Chem. Soc.* **2021**, *143*, 7351; e) Q. Hao, Z.-J. Li, B. Bai, X. Zhang, Y.-W. Zhong, L.-J. Wan, D. Wang, *Angew. Chem., Int. Ed.* **2021**, *60*, 2.
- [14] a) J. W. Colson, A. R. Woll, A. Mukherjee, M. P. Levendorf, E. L. Spitzer, V. B. Shields, M. G. Spencer, J. Park, W. R. Dichtel, *Science* **2011**, *332*, 228; b) Y. Zhong, B. Cheng, C. Park, A. Ray, S. Brown, F. Mujid, J.-U. Lee, H. Zhou, J. Suh, K.-H. Lee, A. J. Mannix, K. Kang, S. J. Sibener, D. A. Muller, J. Park, *Science* **2019**, *366*, 1379.
- [15] R. Li, K. Li, G. Wang, L. Li, Q. Zhang, J. Yan, Y. Chen, Q. Zhang, C. Hou, Y. Li, H. Wang, *ACS Nano* **2018**, *12*, 3759.
- [16] a) R. J. Mortimer, J. R. Reynolds, *J. Mater. Chem.* **2005**, *15*, 2226; b) Y. Wang, E. L. Rønnerstrom, D. J. Milliron, *Annu. Rev. Chem. Biomol. Eng.* **2016**, *7*, 283.
- [17] K. Madasamy, D. Velayutham, V. Suryanarayanan, M. Kathiresan, K.-C. Ho, *J. Mater. Chem. C* **2019**, *7*, 4622.
- [18] S. Wang, J. Xu, W. Wang, G.-J. N. Wang, R. Rastak, F. Molina-Lopez, J. W. Chung, S. Niu, V. R. Feig, J. Lopez, T. Lei, S.-K. Kwon, Y. Kim, A. M. Foudeh, A. Ehrlich, A. Gasperini, Y. Yun, B. Murmann, J. B. H. Tok, Z. Bao, *Nature* **2018**, *555*, 83.
- [19] a) T. G. Yun, D. Kim, Y. H. Kim, M. Park, S. Hyun, S. M. Han, *Adv. Mater.* **2017**, *29*, 1606728; b) W. Kang, M.-F. Lin, J. Chen, P. S. Lee, *Small* **2016**, *12*, 6370.
- [20] H. Ling, J. Wu, F. Su, Y. Tian, Y. J. Liu, *Nat. Commun.* **2021**, *12*, 1010.
- [21] X. Jia, E. C. Baird, J. Blochwitz-Nimoth, S. Reineke, K. Vandewal, D. Spoltore, *Nano Energy* **2021**, *89*, 106404.
- [22] A. Kovács, J. Cz. Dobrowolski, S. Ostrowski, J. E. Rode, *Int. J. Quantum Chem.* **2017**, *117*, e25358.
- [23] D. G. A. Smith, L. A. Burns, K. Patkowski, C. D. Sherrill, *J. Phys. Chem. Lett.* **2016**, *7*, 2197.
- [24] a) D. Singh, S. K. Gupta, Y. Sonvane, I. Lukačević, *J. Mater. Chem. C* **2016**, *4*, 6386; b) H. Li, C. Paolucci, I. Khurana, L. N. Wilcox, F. Göttl, J. D. Albarracin-Caballero, A. J. Shih, F. H. Ribeiro, R. Gounder, W. F. Schneider, *Chem. Sci.* **2019**, *10*, 2373; c) Z. Torbatian, R. Asgari, *Phys. Rev. B* **2018**, *98*, 205407.